Direct Internal Reformation and Mass Transport in the Solid Oxide Fuel Cell Anode: A Pore-scale Lattice Boltzmann Study with Detailed Reaction Kinetics

K. N. Grew[1], A. S. Joshi[1], and W. K. S. Chiu[1]*

[1] Department of Mechanical Engineering, University of Connecticut, 191 Auditorium Rd., Storrs, CT 06269-3139, USA

Abstract

The solid oxide fuel cell (SOFC) allows the conversion of chemical energy that is stored in a given fuel, including light hydrocarbons, to electrical power. Hydrocarbon fuels, such as methane, are logistically favourable and provide high energy densities. However, the use of these fuels often results in a decreased efficiency and life. An improved understanding of the reactive flow in the SOFC anode can help address these issues. In this study, the transport and heterogeneous internal reformation of a methane based fuel is addressed. The effect of the SOFC anode's complex struc-ture on transport and reactions is shown to exhibit a compli-cated interplay between the local molar concentrations and the anode structure. Strong coupling between the phenom-enological microstructures and local reformation reaction rates are recognised in this study, suggesting the extension to actual microstructures may provide new insights into the reformation processes.

Keywords: Heterogeneous Reformation, Lattice Boltzmann Method, Reactive Flow, Solid Oxide Fuel Cell

1 Introduction

Most fuel cells work best with, and often require, hydro-gen fuel. This presents a number of logistical challenges asso-ciated with the storage, transport, and safety of hydrogen fuel [1, 2]. Therefore, it is reasonable to focus on the development of fuel cells that may enable the use of hydrocarbon fuels. Hydrocarbon fuels (e.g. methane) provide high energy densi-ties and specific energies [1, 2]. Further, the public is relative-ly comfortable with them and they are easy to store and trans-port. The benefit of the use of hydrocarbon fuels includes opportunities to use coal syngas [3] and renewable sources from biomass stockpiles [4–6], among others [2, 7]. The effect of the solid oxide fuel cell (SOFC) electrode structure on direct internal reformation and mass transport is of impor-tance to addressing its performance and durability limita-tions. There is a limited understanding of the role of the dis-crete electrode structure on these processes.

The SOFC can use a variety of hydrocarbon based fuels [2, 8, 9]. An examination of the use of a SOFC with a methane fuel is the subject of this study. Light hydrocarbons can effec-tively be used in the SOFC because of the temperature of its operation (e.g., 500–1,000 °C), use of an oxidising ion (i.e. oxide O^{2-}) in the anode, and the use of electrocatalysts and electronic charge carriers in the anode, like nickel (Ni), which can also serve as a catalyst for the internal reformation reac-tions.

In this study, a partially pre-reformed methane fuel in the SOFC is examined. A typical state-of-the-art SOFC anode, which is comprised of a porous nickel/yttria-stabilised zirco-nia (Ni–YSZ), is considered. The Ni serves as an electrocata-lyst, electronic charge carrier and catalyst in the case of an internal reformation process. The YSZ serves as an ionic charge carrier, bringing the oxidising ion into the anode, and the pore regions support the transport of fuel and product species. Electrochemical oxidation occurs in the vicinity of

---

[*] *Corresponding author, wchiu@engr.uconn.edu*

the union of these three materials, or the three-phase boundary (TPB), in the proximity of the anode/electrolyte interface [2]. The use of a hydrocarbon fuel, and specifically methane, has a several-fold effect on the SOFC. First, carbon can coke the active Ni surfaces and result in a degradation of performance [5, 10–13]. Likewise, impurities such as sulphur and phosphorus can poison these catalysts [14]. An improved understanding of the reactive transport in the SOFC electrode structure can help combat these types of issues *via* identification of regions that can promote coking and the effects of local nonlinearities resulting from the detailed structure.

The mass transfer and reformation reactions are coupled to study their effects in detailed microstructures representing the SOFC anode structure in this study. This study is limited to two-dimensional (2D) phenomenological representations of the SOFC anode microstructure. This requires an empirical treatment of the catalytically active area of Ni within the domain. The merits of extending these methods into full 3D structures are discussed. These efforts serves as a precursor to the consideration of carbon coking and oxidation type effects. The development and incorporation of these details is a long-term goal of these efforts. For the present study, a lattice Boltzmann mass transport model is discretely coupled to a detailed reformation reaction mechanism for this effort. Several studies are performed, which include an examination of the effects of the discrete structure considered, catalytically active area and the effect of the methane concentrations in the feed stream. A strong coupling of the structure and reactive transport processes are recognised.

2 Method of Approach

2.1 Structures and Volumes Studied

Several 2D structures are used to represent the SOFC anode. These structures are phenomenological and artificially generated. Each has a controlled porosity, with values ranging from 25 to 50%. Similar representations of the SOFC anode structure have been used in previous studies by the authors [15–17], where they have been used to represent both the full anode support [15, 16] and smaller representative volumes [17]. Here, these structures are used to represent the full anode support. This permits the coupled mass transport and detailed reformation kinetics to be studied. Validation is performed using results from independent studies appearing in the SOFC literature. However, the effect of the microstructure on the coupled transport and reformation reaction processes are also examined on a localised basis.

A schematic of an anode supported planer SOFC is provided in Figure 1(a). Two sub-sections are

noted. First is a projection of a tomographic reconstruction of an actual SOFC anode where the discrete Ni and YSZ phases are noted. These detailed characterisations will enable actual volumes to be considered in future efforts. A phenomenological structure is also shown in Figure 1(a). This provides a representation of the electrode structure that is considered in this study. These structures do not have the complexity of the real anode structures, but they do maintain a porosity that is consistent with actual SOFCs, have been used to validate concentration losses [15, 18], and have tortuosity values of 1.5–2.0 that are consistent with more recent estimates [18–22].

Although phenomenological structures are being used, the authors have an ongoing and complementary effort with the
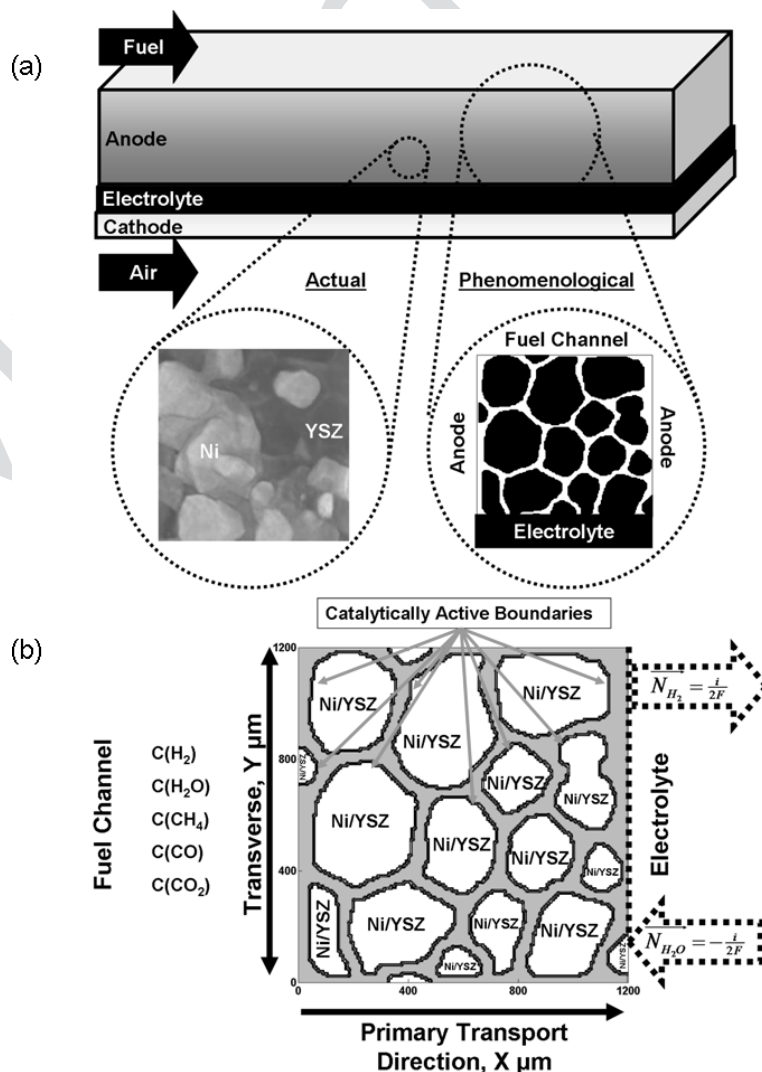
(a)

(b)

Fig. 1 (a) A schematic of the SOFC anode, where a projection of the actual SOFC microstructure is shown along side a phenomenological representation, which uses an empirical correction for the active catalyst area. (b) This structure is used for the direct internal reformation studies, where molar concentrations are specified at $X = 0$ and can diffuse in the grey pore regions. H_2 and H_2O fluxes are specified at $X = 1,220\ \mu m$ using Faraday's law. The dense Ni and YSZ regions of the anode, appearing white in this schematic, are treated with a homogeneous distribution of catalytically active boundary conditions that are representative of the Ni surface. The homogeneous distribution of catalytically active boundaries are scaled to represent a specific catalytically active area.

non-destructive X-ray tomography methods used to image sections of actual SOFC anode microstructures spatial resolutions on the order of 40 nm [19, 20]. These methods have also been extended to provide elemental mapping with Ni absorption contrast using a synchrotron source [20]. Movies of reconstructed volumes of actual SOFC samples with elemental mapping are available for viewing [23]. Other methods, including stereological methods using a focused ion beam mill with a scanning electron microscope (FIB-SEM), have received considerable attention [22, 24–28]. It is prudent explore the scientific and engineering insight that may be gained by using regions of these structures prior to their extension.

2.2 The Five-Species Lattice Boltzmann Method (LBM)

An *m*-species mass transport model is necessary to study reactive transport within discrete electrode architectures. There are several applicable choices, which include the Stefan-Maxwell [29–32] and Dusty Gas [33] equations. These approaches often rely upon a finite element, difference or volume discretisation of the structure. The computational tractability of these methods becomes a significant consideration when considering actual structures. These methods are typically implicit, and therefore matrix inversion and/or gauss elimination type processes are needed and limit their numeric scalability. Complex geometric structures also raise meshing issues. These issues become paramount when actual structures are considered. The X-ray tomography and FIB-SEM studies demonstrated in the literature typically consider volumes on the order of 10^3–25^3 μm^3 with spatial resolutions on the order of 10–50 nm [19, 20, 22, 24–28]. Larger volumes (e.g. >50^3 μm^3) are possible with stitching methods and/or additional characterisation and processing times.

The lattice Boltzmann method (LBM) is used in this study. LBM is an explicit time marching scheme, where a given lattice point is only dependent upon its direct neighbours. This permits a nearly linear scalability using domain decomposition algorithms [16, 18, 34, 35]. The method uses a discretisation of a statistically based, but more fundamental form of the transport equations (i.e. the Boltzmann equation); therefore, LBM can use a regular mesh with high grid independence [34]. LBM is not without drawbacks, this nascent technique requires non-dimensional scaling, low Mach number approximations and conservative boundary conditions to be developed.

LBM is particularly amenable to complex physical structures, like those of the X-ray tomography and FIB-SEM. This is because of LBM's high mesh fidelity nearly linear scalability. For example, pervious reports of a 3-component version of the algorithm on an 81^3 voxel^3 mesh takes approximately 1 week to run on 8 processors [18]. At resolutions typical of X-ray tomography and FIB-SEM methods (i.e. approximately 50 nm), 25^3–50^3 μm^3 volumes are tractable with modern high performance computing facilities; however, cubic decomposition schemes and other optimisations are required. For example, with voxels on the order of 50 nm per edge, a 500^3 and $1,000^3$ voxel^3 (i.e. 25^3–50^3 μm^3, respectively) would take 1 and 8 weeks, respectively on 2,000 processors, respectively. These figures are well within modern and accessible computational facilities and assumes a linear speedup, with processors, which is not an unreasonable approximation even at high processor counts [35].

A five-species LBM is used, representing H_2, H_2O, CH_4, CO and CO_2 mass transfer in a partially reformed methane stream. The stream can undergo direct internal heterogeneous reformation. Details on the development of the multi-component LBM algorithm have been reported previously by the authors [34]. Unique approaches to this problem have also been demonstrated [36, 37]. Only a brief synopsis is provided here.

The basic LBM algorithm provides a discretisation of the Boltzmann equation, onto a discrete lattice. A Bhatnagar–Gross–Krook (BGK) type collision term is used to relax the system towards a linearised form of the Maxwellian equilibrium distribution,

$$f_i^a(\vec{+e_i^a}, t + 1) - f_i^a(\vec{,}t) = \Omega_i^a \qquad (1)$$

where a particle distribution function (PDF) f_i^a, represents the number of 'particles' of species, i, travelling in unit direction, a. The 2D domain maintains 9-directions, which includes a zero position. In Eq. (1), the PDF is updated, based upon its value at the previous time step, where $\vec{e_i^a}$ is a fixed velocity for the movement of particles of species, i, travelling with in unit direction, a. The BGK relaxation term, Ω_i^a, is a relation between the PDF at time, t, and the Maxwellian distribution.

The multi-species model uses fixed velocities, $\vec{e_i^a}$, that are scaled relative to that for the lightest species. The lightest species, H_2, is designated as the first species. The fixed lattice velocity of the heavier species is calculated using the root of the ratio of the species molecular weights $(\vec{e_i^a} = \vec{e_1^a} \cdot \sqrt{MW/MW_i})$. The heavier species stream off-grid and a bilinear interpolation scheme is used to interpret the PDF values on the original lattice. The collision term, Ω_i^a, represents a series of relaxation processes.

$$\Omega_i^a = \left(\frac{f_i^a - f_i^{a(0)}}{\tau_i^v} \right) + \sum_{\substack{j=1 \\ i \neq j}}^m \Omega_{i,j}^a \qquad (2)$$

Separating the self- and cross-collision processes, the first group of terms represents self-collision processes. It is tantamount to viscous processes described by Stokes Law. This Stokes-level description of viscous transport, considers the relaxation of the PDF, f_i^a, *versus* the species equilibrium, Maxwellian PDF, $f_i^{a(0)}$ [34]. The step size of the self-collision relaxation in the LBM analysis is controlled by the viscous relaxation time, τ_i^v. It is related to an LBM kinematic viscosity, v_i, according to $v_i = (2\tau_i^v - 1)/6$. It can be scaled *via* its Reynolds number; however, these contributions are negligible in this study.

The cross-collision terms in Eq. (2) describe inter-molecular collisions that are characteristic of molecular diffusion. Binary relaxation times, $\tau_{i,j}^D$, are used to relax these processes. These relaxation times can be related to the binary molecular diffusion coefficient, $D_{i,j}$, which takes the form of, $D_{i,j} = (\rho P / n^2 MW_i MW_j)[\tau_{i,j}^D - (1/2)]$. The species molecular weights, MW_i, total number density, n, total density, ρ and pressure, P, are needed to define these relaxation times. The pressure is defined in terms of the density and speed of sound in each species, $P = \sum \rho_i c_{s,i}^2$.

The species number density and velocity are determined using moment closures.

$$n_i = \sum_{a=0}^{9} f_i^a \quad \text{and} \quad n_i \vec{u_i} = \sum_{a=0}^{9} f_i^a \vec{e_i^a} \tag{3}$$

The total number density, n, and mass average velocity, $\vec{u_i}$, are calculated in a traditional form manner, $n = \sum_{i=1}^{m} n_i$ and $\rho \vec{u} = \sum_{i=1}^{m} \rho_i \vec{u_i}$, where the density, $\rho_i = MW_i n_i$.

The multi-species LBM algorithm bilinearly back-interpolates the PDF values of the heavier species. To improve accuracy, a *tuned* molecular weight is used [34]. For the five-species mass transport model, this tuning specifies the molecular weight of the heavier species using the first species (i.e. the lightest species), which is set to 1.0 by default.

$$\frac{MW_1}{MW_2} = \frac{D_{2,3}}{D_{1,3}}; \quad \frac{MW_1}{MW_3} = \frac{D_{3,2}}{D_{1,2}}; \quad \frac{MW_1}{MW_4} = \frac{D_{4,2}}{D_{1,2}}; \quad \frac{MW_1}{MW_5} = \frac{D_{5,2}}{D_{1,2}} \tag{4}$$

The *tuned* molecular weights can be set by using the physical molecular diffusivities, predicted by rigorous Chapman–Enskog theory [32, 38]. The diffusivities in the LBM are set using $D_{1,2}$ as a reference, which is the largest diffusion coefficients. It is selected such that cross-collisions relaxation time terms, $\tau_{i,j}^D$, will be on the order of 1.

The diffusion coefficients that are used for the case studies in this work are provided in Table 1. Above the matrix diagonal are the five physical binary diffusion coefficients, calculated using Chapman–Enskog theory. These molecular masses of the respective species are provided in parenthesis. The corresponding tuned molecular weights and LBM diffusion coefficients for these same species are provided below

Table 1 Molecular diffusivities. Champman-Enkskog binary diffusion coefficients are provided above the diagonal. The LBM diffusion coefficients are provided below the diagonal. Respective molecular weights (MW) are provided in parenthesis.

Chapman Enskog theory (MW) / cm² sec⁻¹				
Species	H₂ (2)	H₂O (18)	CH₄ (16)	CO (28)	CO₂ (44)
[0,1-6]LBM (MW) / lu² lt⁻¹				
■H₂ (1.000)	–	7.6577	6.1992	6.4194	5.5312
■H₂O (2.667)	0.7658	–	2.3242	2.2162	1.7242
■CH₄ (3.295)	0.6199	0.2324	–	1.9595	1.5961
■CO (3.454)	0.6419	0.2216	0.1960	–	1.4074
■CO₂ (4.400)	0.5531	0.1724	0.1596	0.1470	–

the matrix diagonal in Table 1. These represent the values that are used for these studies.

Concentration and flux boundary conditions are required to implement the LBM algorithm. The PDF must be manipulated so that the moment closes in Eq. (3), recover the appropriate concentrations and velocities to obtain these boundary conditions. We define a second species velocity, $\vec{u_i^-}$, which is consistent with the methods reported by Shan and Doolen [39]. This second species velocity is related to the molar flux, $J_i = n_i \vec{u_i}$. To define this second velocity for five-species LBM algorithm, a moment closure is used.

$$8n_i \vec{u_i} = \left(8 - \sum_{\substack{j=1 \\ i \neq j}}^{5} \frac{1}{\tau_{i,j}^D} \right) \sum_{a=0}^{8} f_i^a \vec{e_i^a} + \left(\sum_{\substack{j=1 \\ i \neq j}}^{5} \frac{1}{\tau_{i,j}^D} \right) \sum_{a=0}^{8} f_i^{a(\text{eq.})} \vec{e_i^a} \tag{5}$$

The concentration and flux boundary conditions can be defined using Eqs. (3) and (5), to specify the unknown PDF values. For a concentration boundary condition, n_i, is specified the species velocity from the previous time-step is used. For a flux boundary, the local concentration from the domain, n_i, is read and the species velocity is specified to satisfy the flux condition. A bounce-back procedure is additionally used for impermeable no-slip boundaries, which is first order accurate. The use of a second order zero-slip boundary condition will be left for future work and should result in improvement in both convergence and mass balance.

2.3 Detailed Reformation Kinetics

The use of detailed heterogeneous reaction kinetics, which describes the reformation processes, is a key aspect of this study. A mechanism proposed and validated by Hecht et al. [40] is used to describe these reactions. This mechanism has received considerable attention [8, 40–47], which is evidence of its fidelity. There are extensive discussions on the development, details, limitations and the use of this mechanism available; therefore, only select aspects are discussed here.
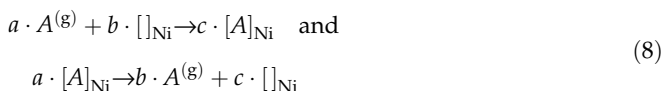
In the study by Hecht et al. [40], validation is provided using several rather elegant experiments that permit independent control of species concentrations, temperature and volumetric flow rates, and provides validation over a ranger of inputs and conditions. This experimental effort contains details of water-gas shift and steam reformation reactions that are often treated on an equilibrium basis.

$$CH_4 + H_2O \Leftrightarrow 3H_2 + CO \tag{6}$$

$$CO + H_2O \Leftrightarrow H_2 + CO_2 \tag{7}$$

However, no *a priori* assumption is made in their attempt to recover these processes [40]. Their effects are captured as a product of the elementary reactions comprising the mechanism, which is a more fundamental description. The mechanism includes the effects of total and partial oxidation

(CPOX), which occurs in the presence of oxygen. However, this study examines reformation in the oxygen deficient SOFC anode; therefore, the oxidation based contributions are negligible.

The mechanism proposed and validated by Hecht et al. [40] has 42 irreversible elementary reactions, and is used in its complete form. A schematic of the mechanism is provided in Figure 2(a). There are up to six-species that can undergo adsorption and desorption on the Ni catalyst surface.

$$a \cdot A^{(g)} + b \cdot []_{Ni} \rightarrow c \cdot [A]_{Ni} \quad \text{and}$$

$$a \cdot [A]_{Ni} \rightarrow b \cdot A^{(g)} + c \cdot []_{Ni} \tag{8}$$

On the catalyst surface, there are 12 unique surface intermediates. These intermediates can propagate through a series of 30 irreversible elementary surface reactions.

$$a \cdot [A]_{Ni} + b \cdot [B]_{Ni} \rightarrow c \cdot [C]_{Ni} + d \cdot [D]_{Ni} \tag{9}$$

It is carefully noted by Hecht et al. [40] that the mechanism includes carbon and oxygen coverage terms; however, it has not been validated for coking or Ni oxidation conditions at this time. We will consider the extension of this mechanism to include these types of effects in future efforts.

To solve the kinetic mechanism, a pseudo-steady state approximation (PSSA) is used, which states that the net formation of all surface-intermediate species is negligible. A mass balance is performed on each of these surface intermediate species, which equates the rate of generation and destruction of each species *via* the various elementary reactions. There are 12 coupled nonlinear equations. An additional Ni vacancy intermediate is used for closure. The surface species are solved in terms of a species surface coverage, θ_i, which corresponds to the ratio of the individual surface concentration to the catalytically active site concentration, $\Gamma_{Ni} = 2.6 \times 10^{-9}$ mol cm^{-2} [46].

The rates of the heterogeneous reformation reactions can occur on significantly different time scales, which create a numerically stiff problem. A globally convergent Newton method is used to solve the nonlinear system of equations representing the heterogeneous reaction kinetics in this study [48]. A line-search algorithm is used to ensure that the function adequately decreases with an option for backtracking along the Newton direction. The Jacobian matrix is explicitly defined to improve stability. An initial guess is required for solution. The surface coverage values predicted at a particular lattice point are stored for use as initial guesses for subsequent time steps. The net rates of adsorption or desorption (flux) are calculated for each species using their respective elementary reactions using the roots of the system.

2.4 Reactive Mass Transfer

Non-dimensional scaling must be used to couple the LBM mass transport to the detailed heterogeneous reformation reaction kinetics. When scaled, the detailed reformation reactions can be implemented as discrete boundary condition within the LBM model, permitting localised concentrations and fluxes within the LBM and reformation models to synchronise in a consistent manner. The scaling must be consistent with the scaling of the electrochemical oxidation of H_2 to H_2O *via* Faraday's law.

A schematic of the structure, and required boundary conditions, are provided in Figure 1(b). Concentration boundaries are required for describing the species concentrations at the domain inlet, representative of the fuel channel. Unique flux boundary conditions are used to (i) treat the flux of H_2 and H_2O, according to Faraday's law at the anode/electrolyte interface, and (ii) the fluxes resulting from the reformation reactions. The Fara-
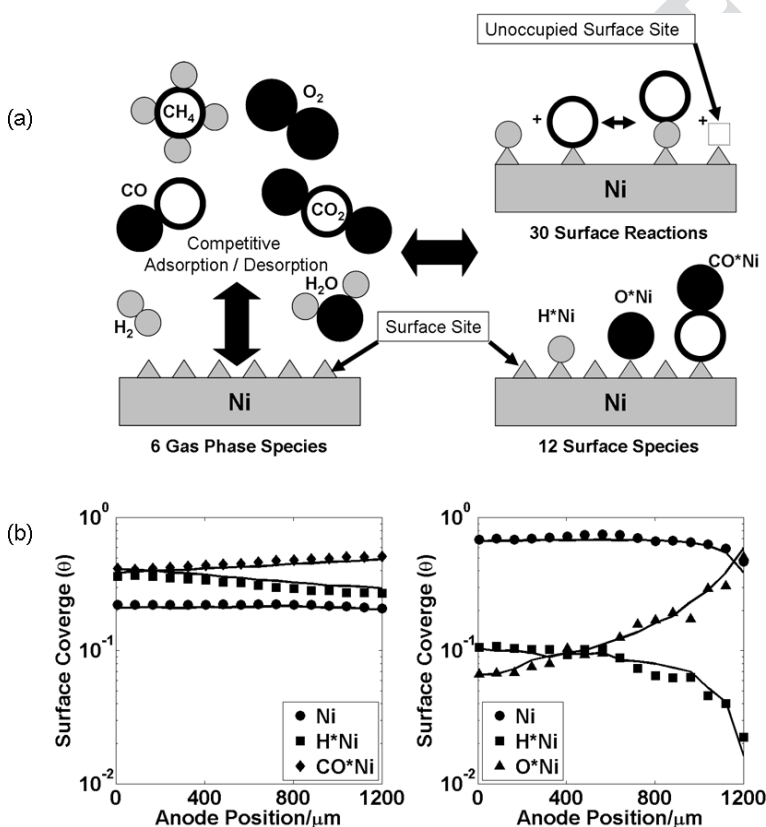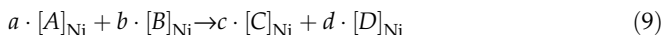

Fig. 2 (a) A Schematic of the reformation reaction kinetics proposed by Hecht et al. [40] is shown. Six gas-phase species competitively adsorb and desorb from available surface sites on the catalyst, Ni, surface. Once adsorbed, there are 12 intermediate surface species along with unoccupied sites. These intermediate surface species are governed by 30 surface reactions. (b) The implementation of this mechanism is verified, where dominant surface species surface coverage values (symbols) are compared to those reported by Zhu et al. [46] (lines). These verifications use gas concentrations interpreted from Ref. [46]. The scatter of the predicted surface concentrations is a product of the sensitivity of the model to the gas concentrations obtained from Ref. [46].

daic flux of H_2 and H_2O are treated on a total basis in this study, $\overrightarrow{J_{H_2}} = -\overrightarrow{J_{H_2O}} = \overrightarrow{i}/2F$, where the cell's current density, $\overrightarrow{i}$, and Faraday's constant, F, are used. The reformation reactions are treated on a discrete basis at the solid/pore interface. Each lattice interface that is prescribed with a reformation boundary condition has a full and independent set of detailed reaction kinetics attributed to it.

The non-dimensional scaling used for this study begins with the introduction of a non-dimensional flux, J^*, for the Faradaic processes.

$$J^* = \frac{J_{H_2}^{Far} L}{C_T D_{1,3}} \tag{10}$$

It is defined using the H_2 flux from Faraday's law, $J_{H_2}^{Far}$, domain length, L, total concentration, C_T, and binary diffusion coefficient for H_2 and CH_4, $D_{1,3}$ [15–18, 34].

The fluxes from the detailed heterogeneous reformation reactions require treatment of the catalytically active area. There are N_{Active}^{Ref} boundaries at the solid/pore interface in the LBM domain that are catalytically active, which are set in the geometry input file. To maintain a physical reference frame, these boundaries must be scaled so that a catalytically active area that is representative of an actual SOFC is obtained. In the SOFC, these catalytically active areas have been experimentally measured [20, 22, 24], estimated using artificial structural generation routines [49, 50], and calculated using percolation theory [51, 52]. To use an appropriate catalytically active area, a second non-dimensional scaling parameter, A^*, is required.

$$A^* = (A_{Ni-Pore} L)_{phys} = A_{Coef} \left(\frac{N_{Active}^{Ref}}{L \cdot H \cdot D} \cdot L \right)_{LBM}$$

$$= A_{Coef} \left(\frac{N_{Active}^{Ref} \cdot N_x}{N_x \cdot N_y \cdot 1} \right)_{LBM} \tag{11}$$

This non-dimensional parameter provides a measure of the catalytically active area. It is the defined as the product of the area of the Ni–pore interface per unit sample volume, $A_{Ni-Pore}$, and the anode length, L. In the LBM studies it is based upon the product of the number of lattice points comprising length of the domain, N_x, and the number interface boundaries for the reformation reaction, N_{Active}^{Ref}. This product is normalised by the volume of the LBM domain, $N_x \cdot N_y \cdot 1$, where unit depth is implied for the 2D study.

To simplify the implementation of A^* in the LBM a constant coefficient, A_{Coef}, is defined. A_{Coef} equates the magnitude of A^* between the physical and LBM reference frames. The flux calculated by the heterogeneous reformation reactions is scaled by A_{Coef} when implemented into the LBM. Additionally, the discrepancies between the physical reaction rates and the unique LBM units are resolved by scaling these fluxes using the ratio of the Faradaic H_2 flux used in the LBM model to that of the actual Faradaic flux.

$$\overrightarrow{J}_{LBM}^{Ref}(x,y) = A_{coef} \left(\frac{J_{H_2}^{Far}\big|_{LBM}}{J_{H_2}^{Far}\big|_{Phys.}} \right) \cdot \overrightarrow{J}_{Phys}^{Ref}(x,y) \tag{12}$$

This ratio is used to scale the flux calculated by the heterogeneous reformation reaction mechanism. The position coordinates are included because the flux occurs uniquely at each active interfacial lattice point.

2.5 Mole Balance

As a check on the quality of the solution procedure, a formal definition for a mole balance across the computational domain is provided in Eq. (13). The magnitude of difference of the mole entering/leaving the domain at the inlet, relative to those that are produced/consumed *via* the reformation and Faradaic reactions are scaled relative to the magnitude of the net conversion for the reformation and Faradiac reactions.

$$\%Error = 100\% \times \left[\frac{\left| \sum_{i=1}^{5} \overrightarrow{J_i^{In}} - \left(\sum_{i=1}^{5} \overrightarrow{J_i^{Ref}} + \sum_{i=1}^{5} \overrightarrow{J_i^{Far}} \right) \right|}{\sum_{i=1}^{5} \left| \overrightarrow{J_i^{Ref}} \right| + \left| \overrightarrow{J_{H_2}^{Far}} \right|} \right] \tag{13}$$

The reformation and Faradiac fluxes are denoted as positive for leaving the domain and the fluxes along the domain inlet at $X = 0$ are positive for a flux entering the domain. For the cases considered in this study, the reformation rates were found to span two to three orders of magnitude, which straddle the magnitude of the Faradaic reactions. Therefore, Eq. (13) scales the error relative to the net conversion from the reactive processes and provides the objective definition of a mole balance. For all cases considered, a net mole balance exhibited 5% difference maximum, with most cases being less than 2%.

3 Verification and Validation

3.1 The Five-Species LBM

The five-species LBM is validated by considering diffusion in a simple 1D channel. The Stefan-Maxwell equations, which are valid for *m*-component continuum transport, are used for comparison.

$$\nabla x_i = \sum_{j=1}^{m} \frac{1}{C_T D_{i,j}} (x_j \overrightarrow{N_i} - x_i \overrightarrow{N_j}) \tag{14}$$

In the Stefan-Maxwell equations, the gradient of the mole fraction of species i, x_i, molar flux, $\overrightarrow{N_i}$, total concentration, C_T and binary diffusion coefficients, $D_{i,j}$, are used to form a set of *m*-equations. Volumetric generation and/or destruction of species are neglected.

Three validation cases are considered. These cases are described in Table 2, and include (i) equimolar counter-diffusion of two species, (ii) unique fluxes on all five species with

Table 2 Validation of the five-species LBM with the Stefan-Maxwell equations. All cases use a non-dimensional H_2 flux, $J^* = 0.139$.

[1,0]Case	[1,0]Species	[1,0]Flux / mol m^{-12} sec^{-1}	[1,0]Mole fraction, $z = 0$	[0,5-6]Mole fraction, $z = L$		[1,6-7]% Difference
				Stefan Maxwell	Lattice Boltzmann	
[5,0]1	H_2	+1.000	0.5	0.375	0.381	0.5
	H_2O	-1.000	0.1	0.320	0.309	1.4
	CH_4	-	0.2	0.158	0.158	0.5
	CO	-	0.1	0.077	0.078	0.7
	CO_2	-	0.1	0.070	0.073	1.6
	Net	0.000	1.0	1.000	1.000	0.0
[5,0]2	H_2	+1.000	0.5	0.364	0.372	0.2
	H_2O	-0.750	0.1	0.257	0.249	0.9
	CH_4	+0.250	0.2	0.076	0.078	3.1
	CO	+0.125	0.1	0.033	0.037	5.3
	CO_2	-0.625	0.1	0.271	0.265	1.0
	Net	0.000	1.0	1.000	1.000	0.0
[5,0]3	H_2	+1.000	0.5	0.423	0.428	0.1
	H_2O	-0.250	0.1	0.179	0.177	0.1
	CH_4	+0.500	0.2	0.055	0.053	3.2
	CO	+0.250	0.1	0.020	0.024	2.5
	CO_2	-0.500	0.1	0.323	0.320	0.9
	Net	1.000	1.0	1.000	1.000	0.0

no net flux and (iii) unique fluxes on all five species with a net molar flux of 1.0 mol m^{-2} sec^{-1} out of the domain. All three cases consider the same concentration boundary conditions, domain length, $L = 1,000$ µm or 50 lattice units (lu), and non-dimensional flux, $J^* = 0.139$. Results from these validations are provided in Figure 3. The Stefan-Maxwell results (lines) compare favourably to the LBM results (symbols) for all three cases. Some minute discrepancy arises in the latter two cases, which are highlighted in Table 2. These percentage differences are defined relative to the Stefan-Maxwell solutions. The largest percent differences occur for the with ■Please verify or modify the sentence for clarity.■species smallest mole fractions at $X = L$, amplifying the error. The agreement between the two methods provides confidence in the use of LBM to describe multi-component mass transport.

3.2 Detailed Reformation Kinetics

The implementation of the reaction kinetic mechanism and associated solution procedure are validated using results published by Zhu et al. [46]. The results published by Zhu et al. provide both species mole fractions and surface coverage values along the anode support. These results serve as detailed annotations of the coupled effect of mass transfer, Faradaic processes, and the reformation reactions at unique locations along a planar SOFC.

To validate the implementation of the reaction kinetics model, the mole fractions along the length of the anode support in Ref. [48] are used as inputs to a stand-alone version of the reformation reaction kinetics model to predict the associated species surface coverage values. Results are compared to those reported by Ref. [46] for several of the dominant surface species. The results from this comparison in surface species are provided in Figure 2(b), where the values from Ref. [46] are represented with solid lines and those predicted for this verification are denoted with symbols. The agreement between the two provides confidence in the implementation of the kinetics. The scatter in species surface coverage values that we have calculated, compared to those of Ref. [46], is a result of our inability read the local mole fractions in Ref. [46] with sufficient precision. The species surface coverage values we predict bracket those interpreted from Zhu et al. [46], providing confidence in the implementation of the kinetics.

3.3 Coupled Mass Transport and Reformation Kinetics

The entire coupled mass transport and reformation reaction system is validated by comparison to independent results reported by Janardhanan and Deutschmann [53]. The cell considered in this study is described as having a porosity of $\varepsilon = 35\%$, tortuosity factor of $\tau^2 = 3.8$, anode length of $L = 500$ µm, and active catalyst area of $A_{Ni-Pore} = 1.025 \times 10^5$ m^{-1}.
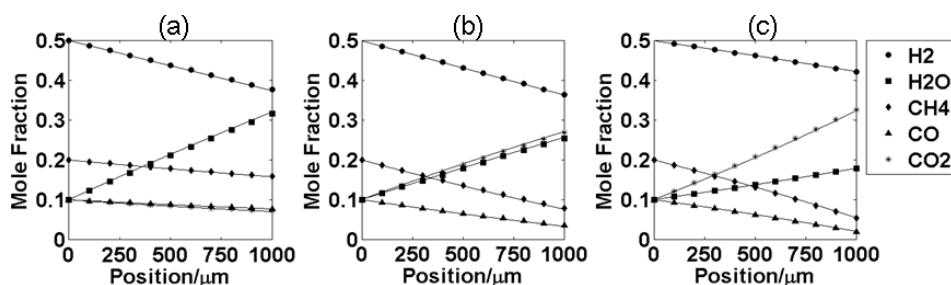

Fig. 3 The five-species LBM (symbols) is validated using the Stefan-Maxwell equations (lines) for mass transport in 1D channel, for the conditions provided in Table 2. These include (a), Case 1, equimolar counter-diffusion of H_2 and H_2O with all remaining species being inert effluent, (b.) Case 2, unique fluxes applied to all five-species with no net molar flux, and (c.) Case 3, unique fluxes applied to all five-species with a net molar flux, $N_t = 1$ mol m^{-2} sec^{-1}. Consistent inlet species concentrations and $J^* = 0.139$ are considered.

There are several intricacies to this validation. Janardhanan and Deutschmann [53] do not consider an isothermal model; however, temperature gradients between the fuel channel and electrolyte are not substantial. Therefore, an average temperature of $T = 1,025$ K is used for the purposes of validation in this study. Second, we neglect Knudsen diffusion processes. At the temperatures and pore-radii reported, this will result in some modest errors [53, 54]. The effects of Knudsen diffusion should impede transport and result in larger concentration gradients. This is more pronounced for the species with larger molecular weights, which have a lower Knudsen diffusion coefficient. This will introduce some error into the LBM mass transfer and coupled heterogeneous reformation reaction results. It is accepted at this time as a limitation of the present study.

Finally, in actuality unique structures are considered. Janardhanan and Deutschmann [53] consider a porosity and tortuosity factor of $\varepsilon = 35\%$ and $\tau^2 = 3.8$, respectively. This provides a porosity–tortuosity factor, $\Psi = 0.35/3.8 = 0.0921$, representing the resistance of the structure to mass transport. The tortuosity factor was called a tortuosity, but has been elucidated in several recent discussions [21, 55, 56] and not commented on further here. The discrete structure that is used for validation in this study has unique properties. It has a nominal porosity of $\varepsilon = 35\%$ and a tortuosity of $\tau = 1.73$, which correspond to a porosity–tortuosity factor of, $\Psi = 0.117$. The length of the anode considered in the non-dimensional scaling parameters J^* and A^* is extended to account for this discrepancy. Recognising that the length used in these scaling parameters, $\tilde{L}$, can be corrected using the actual anode length, L_{an}, and the ratio of the porosity–tortuosity factors considered by Janardhanan and Deutschmann and that for the structure used in this study, or $\tilde{L} = L_{an}(\Psi_{Janardhanan}/\Psi_{Structure})$.

With these assumptions, three validation cases are considered in Figure 4. Results extracted from Ref. [53] (symbols) are compared to the coupled LBM and heterogeneous reformation kinetic model (lines). The scatter-bars provided with the LBM results correspond to the bounding mole fractions in determined in the transverse-Y direction (i.e. the Y-direction from Figure 1(b)). These scatter-bars bound the data from Ref. [53], with some modest exceptions. The three validation
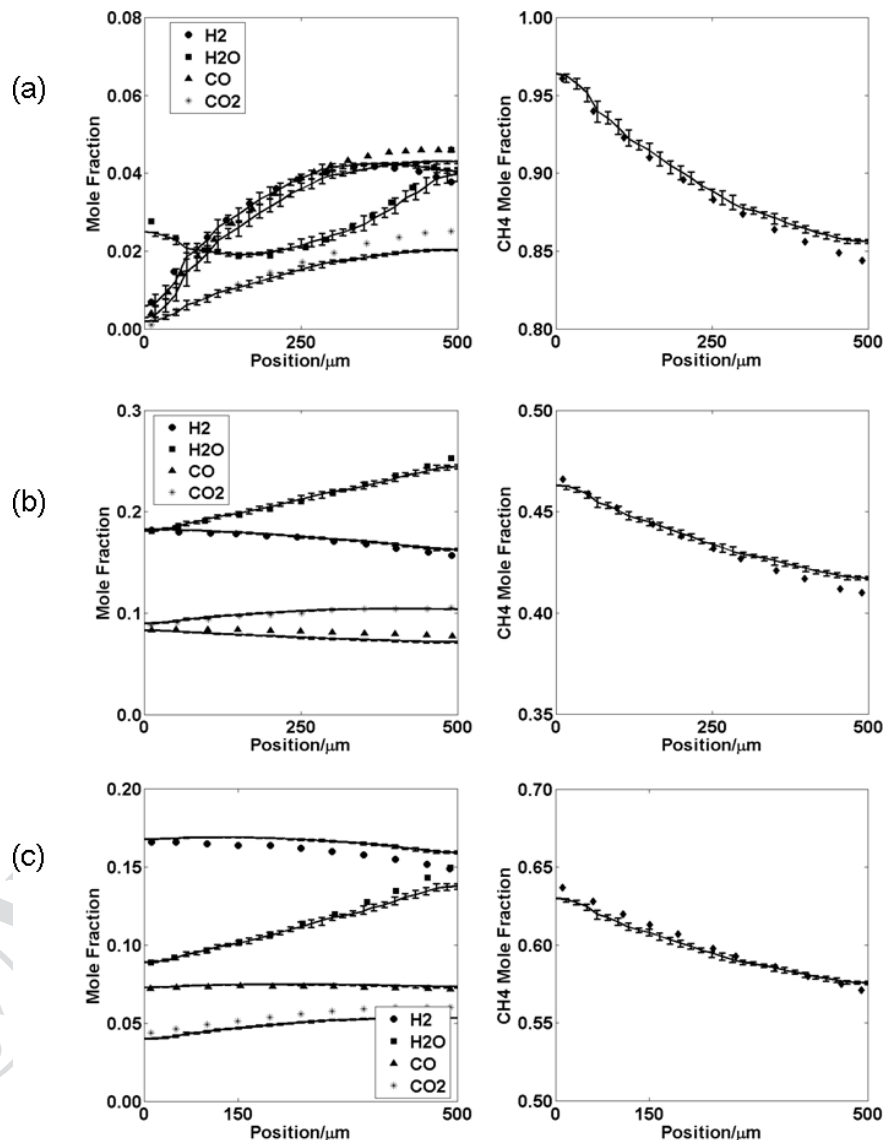

Fig. 4 The validation of the lattice Boltzmann mass transport model with the coupled heterogeneous reformation kinetics, where the lattice Boltzmann results (lines) are compared to results from Janardhanan and Deutschmann [53] (symbols). The scatter-bars represent the transverse variation in the mole fractions between the SOFC fuel channel and electrolyte, at positions 0 and 500 μm, respectively. Current densities of, (a) $i = 0.69$ A cm^{-2}, (b) $i = 0.81$ A cm^{-2} and (c) $i = 1.03$ A cm^{-2} are shown.

cases presented in Figure 4 represent current densities of Figure 4(a) 0.69 A cm^{-2}, Figure 4(b) 0.81 A cm^{-2} and Figure 4(c) 1.03 A cm^{-2}. These cases are taken from different locations along the fuel channel of the same cell, requiring unique concentration and Faradaic flux boundary conditions. The agreement between the results of Ref. [53] provides confidence in the implementation of the reactive transport model.

4 Results and Discussion

With confidence in the model, several studies are considered. Specifically, the effects related to the consideration of

Table 3 SOFC anode properties considered in the respective case studies.

Case	Independent property	Value(s)	Current density / A cm^{-2}	Catalytic area / µm^{-1}	Porosity	Length / µm
1	Porosity (tortuosity)	0.25, 0.30, 0.35, 0.40, 0.45, 0.50	2.0	0.108	–	1,220
2	Catalytic area	0.10, 0.25, 0.50, 0.75, 1.00 / µm^{-1}	2.0	–	0.35	1,220
3	Inlet CH_4 Mole fraction	0.1, 0.2, 0.3, 0.4, 0.5 (CH_4+H_2 = 0.60)	2.0	0.750	0.45	1,220

the discrete electrode structure are explored. This is a key difference between the present study and those that have been reported using homogenised volume averaging methods [8, 40–47]. The parametric studies are broken down into three cases, described in Table 3. The first two are derived from the same base case, which uses conditions discussed in Ref. [46]. The final case takes uses some unique properties, which are still representative of state-of-the-art SOFC anodes, to demonstrate the unique capabilities of the discrete pore-scale approach.

4.1 Porosity and Tortuosity

The effect of the porosity and tortuosity of the structure on transport are considered using six unique structures. These structures have nominal porosity values of ε = 25, 30, 35, 40, 45 and 50%, which have tortuosity values of τ = 2.2, 1.7, 7.7, 1.5, 1.4 and 1.2, respectively. The tortuosity values are calculated using a structural factor, $\Psi = \varepsilon / \tau^2$, evaluated using a solution to Laplace's equation in the domain. These methods are reported elsewhere [18, 21].

The effect that these discrete structures have on the reactive transport is shown in Figure 5. The mean mole fractions

of Figure 5(a) H_2, (b) H_2O, (c) CH_4, (d) CO and (e) CO_2 are provided for each of the structures. Arrows in Figure 5 indicate the direction of increasing porosity. This increase in porosity implies a complementary decrease in tortuosity. Combined, these arrows effectively indicate a decrease in the structural 'resistance' to mass transport. The gradients in mole fractions become less significant with a decrease in this structural resistance. Variations in the spanwise-Y direction that result from the consideration of the discrete structure are noted with the scatter-bars. The gradients in mole fraction in the spanwise direction are more pronounced for the structures with an increased resistance to transport.

4.2 Active Catalyst Area

The examination of the catalytically active area on transport and reaction in the SOFC anode is shown in Figure 6. The values selected for this study range between that which was for the validation studies, $A_{Ni-Pore} \approx 1.0 \times 10^5$ m^{-1}, and a value on the order of those that have recently been experimentally measured, $A_{Ni-Pore} \approx 1.0 \times 10^6$ m^{-1} [20, 22]. As with the previous result, the trends are grouped on a species-by-species basis, and arrows are used to indicate the direction of increasing catalytically active area.

Several observations can be made about the results provided in Figure 6. First, the increased catalytic area appears to result in a complementary increase in the conversion of CH_4 and H_2O to H_2, CO, and CO_2. This is not unexpected; however, the monotonic increase with increased catalytic area conversion suggests that these reactions are limited by the heterogeneous reactions. Still, this may be the result of a relatively low H_2O concentration. That is, there is only a sufficient H_2O concentration to support a moderate reformation reaction. An increased H_2O concentration with higher catalytic areas may not have a monotonic dependence.

A grouping of the CO and CO_2 curves for the lowest and highest catalytic areas, respectively, is also observed. This scenario is rather unexpected. The increase in catalytic area enhances the net conversion *via* the heterogeneous reformation processes; however, this grouping suggests that this perturbation in catalytically active area is sufficient to perturb local conditions enough that an observable change in the kinetic regime of the reformation mechanism is observable. This change has altered competitive adsorption/desorption processes and
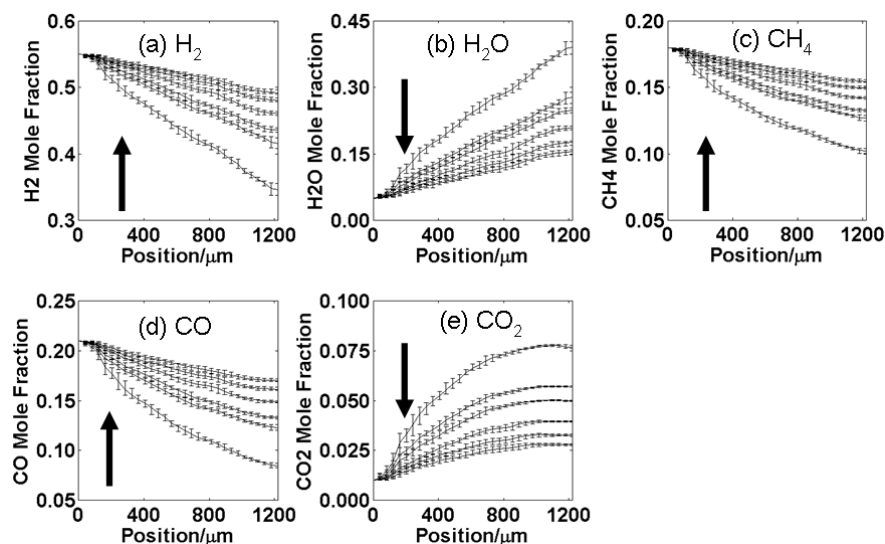

Fig. 5 The effects from the effect of unique porous structures on the reactive transport in the SOFC anode are shown. The arrows indicate the direction of increasing structural porosity from 25 to 50%, which is implicitly accompanied by a decrease in the tortuosity. The scatter-bars represent spanwise-Y variations in species mole fractions. Trends are shown on a species-by-species basis, with (a) H_2, (b) H_2O, (c) CH_4, (d) CO, (e) CO_2 containing each porosity value.
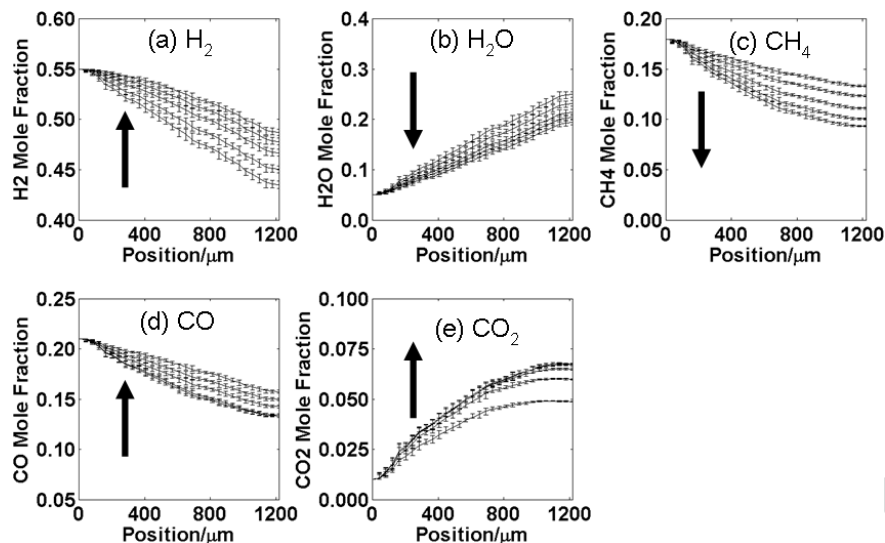
Fig. 6 The effects of the catalytic area, $A_{\text{Ni–Pore}}$, on the reactive transport in the SOFC anode are shown. The arrows indicate the direction of increasing catalytically active area from 1×10^{-5} to 1×10^{-6} m^{-1}. The scatter-bars represent spanwise-Y variations in species mole fractions. Trends are shown on a species-by-species basis, with (a) H$_2$, (b) H$_2$O, (c) CH$_4$, (d) CO, (e) CO$_2$ containing each catalytically active area value.

nificant effect on catalytic activity and magnitude of the heterogeneous reactive processes. After some preliminary studies at conditions consistent with the previous results (not shown), the H$_2$O concentration was increased to amplify its contributions. The impact of both the CH$_4$ and H$_2$O concentrations are exemplified in Figure 7, where the mean species mole fractions are shown for the unique H$_2$ and CH$_4$ balances. As before, the scatter-bars represent the spanwise-Y variations in mole fraction.

Turning our attention to the results in Figure 7, some rather substantial observations can be made. These observations begin with the growing scatter-bars. This increase in spanwise-Y scatter correlates with an increasing inlet CH$_4$ mole fraction. From this, we can conclude that this increased variation is due in large to localised reformation processes. Further, for these variations to present themselves, the transport and reaction processes must be approaching characteristic time scales (i.e. residence times) that are of a comparable order. The discrete structure can further amplify these effects as regions become isolated. While not present in this study, the variations resulting from a dead end pore (i.e. blind) and large voids behind structural constrictions could be augmented in such a sce-
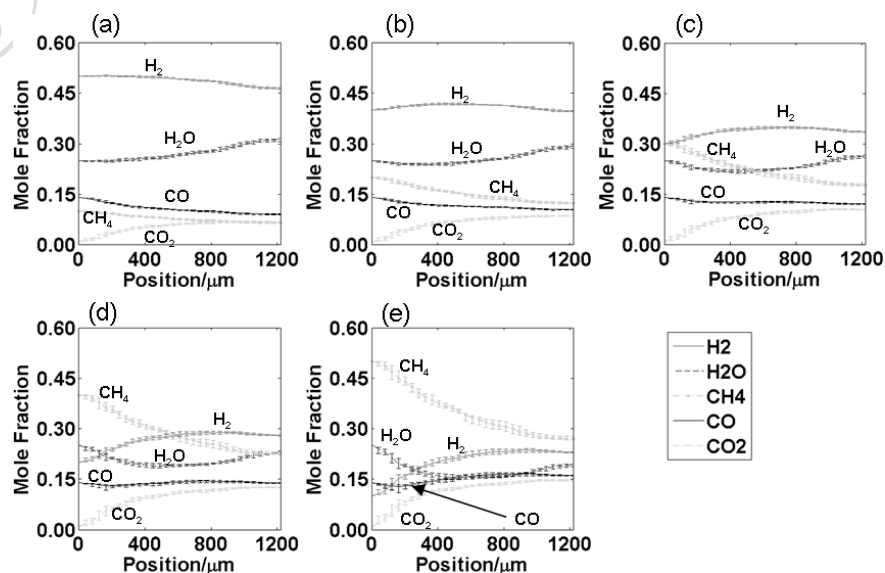
subsequent surface processes that consumption of CO and production of CO$_2$ are saturating at low and high catalytic areas, respectively.

4.3 Fuel Channel Methane Concentration

The final study performed considers unique aspects of the previous studies. Unique species composition at the anodic the fuel channel are also considered. An active catalyst area that is closer in magnitude to the larger of the values that have been reported within the experimental literature, $A_{\text{Ni–Pore}} = 7.5 \times 10^5$ m^{-1}, is used with a current density of, $i = 2.0$ A cm^{-2}. The anode support porosity is considered to be a higher porosity, $\varepsilon = 45\%$, which is representative of high performance anodes that have been demonstrated in the literature [57, 58]. Mole fractions at the fuel channel are set to H$_2$O = 0.25, CO = 0.14, CO$_2$ = 0.01. The H$_2$ and CH$_4$ mole fractions provided the balance and are systematically varied between values 0.1 and 0.5, respectively.

A key aspect of this study is the role of the H$_2$O content. As noted in Eqs. (6) and (7), both the steam reformation and water–gas shift reactions are strongly coupled to the water content. The increase in H$_2$O concentration, along with the higher values of CH$_4$, has a sig-

Fig. 7 The effects of the balance between H$_2$ and CH$_4$ at the fuel channel are examined. Specific cases considered include (a) H$_2$O = 0.5 and CH$_4$O = 0.1, (b) H$_2$O = 0.4 and CH$_4$O = 0.2, (c) H$_2$O = 0.3 and CH$_4$O = 0.3, (d) H$_2$O = 0.2 and CH$_4$O = 0.4, and (e) H$_2$O = 0.1 and CH$_4$O = 0.5. As the CH$_4$ content increases, a more pronounced reformation reaction occurs, resulting in local minima and maxima for the H$_2$O and H$_2$, respectively, towards the middle of the domain. Increased production of CO$_2$ is recognised and CO moves from being consumed to being produced through the respective cases. The scatter bars represent the spanwise-Y variations.

nario. This implies that in these types of cases the pore-scale structure can play a significant role in the reactive transport. The species contour plots provided in Figure 8, which are an expanded view of the results from Figure 7(e), support this claim. In the contour plots for H_2, H_2O and CO Figure 8(a), (b), and (d), respectively, pockets of high species concentration can be observed in the central regions of the structure. These pockets correspond to regions of increased H_2 and CO and decreased H_2O. These regions are localised between groupings of solid structures in an otherwise periodic domain. The result helps confirm the coupling between structure, transport and reaction.

Returning to Figure 7, it can be seen that the magnitude of the CH_4 conversion process increases from the highest inlet H_2 concentration in Figure 7(a) to the lowest inlet H_2 concentration in Figure 7(e). It is not unexpected to see an increase in CH_4 conversion with increased in concentration; however, over the span of these studies, H_2 goes from being consumed by the Faradaic processes, to actually being produced by the CH_4 reformation to the extent that its concentration gradients force it to diffuse in a direction opposite of the Fardaic flux. In these later cases, the SOFC is actually ejecting H_2 back into the fuel channel. Further, examining the mean mole fractions for these later cases, it is quite difficult to detect a gradient in H_2 at the boundary where the Faradaic flux is occurring. A complementary observation can be made for the H_2O, which is being produced at this same boundary. This is indicative that reformation processes in the neighbouring regions are reforming CH_4 in the support with any H_2O that is produced by the Faradaic reaction in these immediately neighbouring regions. The H_2 produced by this process is again consumed by the adjacent Faradaic reaction. This creates a short, closed

loop. This process seems to occur as long as there is sufficient CH_4 and H_2O. This can again be confirmed by examining the H_2, H_2O and CH_4 contour plots in Figure 8(a)–(c), respectively. The various mole fraction plateaus have appear as if they would have normal lines, which correspond to fluxes that occur directly between particles adjacent to the right hand boundary uses that uses a Faradaic flux boundary condition. This demonstrates a coupling between the Faradaic process and the reformation processes at these neighbouring particles. It is interesting to note that this looks very much like a direct oxidation of the CH_4. It appears to have a more significant gradient at this boundary than either the H_2 or H_2O, despite there being no mechanism in place for a direct electrochemical oxidation of CH_4.

One final observation can be made by returning to Figure 7. In the later cases shown in Figure 7, which correspond to an increased inlet CH_4 mole fraction, a minima and maxima in the mole fraction for several of the species occurs in the central regions of the domain. This is most pronounced with the H_2 and H_2O in Figure 7(c) through Figure 7(e). These localised inflections again suggest that the complex interplay between the SOFC anode's microstructure has resulted in the characteristic time scales of transport and reaction being comparable in magnitude.

5 Summary

From the studies performed in this work, role and importance of the porosity and tortuosity of the electrode structure, catalytically active area and species mole fractions at the fuel channel on the direct internal reformation of methane have been examined. Discrete structures have been used for these studies and some expected and un-expected results have been found. As the ratio of the porosity to tortuosity factor decreased in magnitude larger gradients in species mole fractions were observed. This is the direct result of an increased resistance to transport due to a decreased porosity and increased tortuosity. Similarly, it has been found that the conversion of CH_4 and H_2O, which were reformed to H_2, CO and CO_2, increases with catalytically active area. This reformation process results in decreased species gradients across the anode support. However, while H_2, H_2O and CH_4 see a monotonic change in conversion with increased catalytically active area, the CO and CO_2 see several of their trends collapse. At low and high catalytically area, respectively, the CO and CO_2 saw trends collapse. This is indicative of a change in mechanism; likely the product of increased reformation on a local basis.
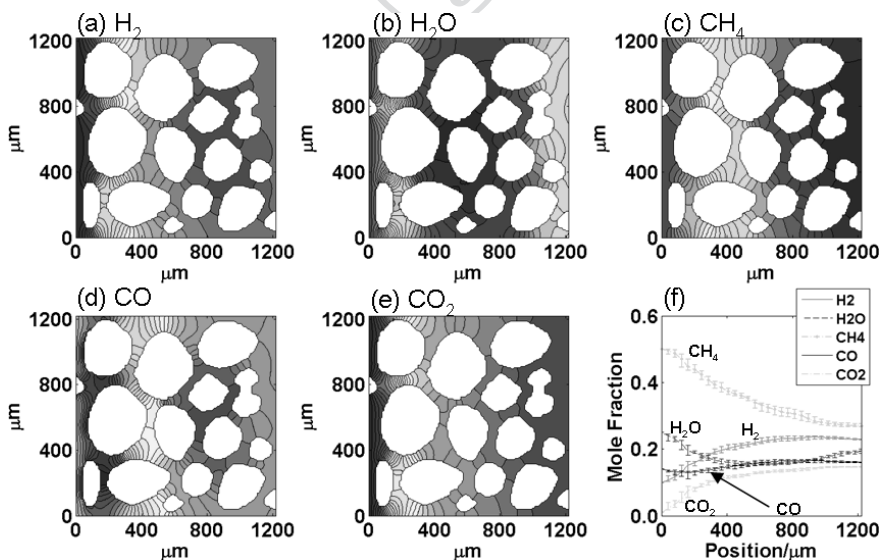

Fig. 8 Contour plots for (a) H_2, (b) H_2O (c) CH_4, (d) CO and (e) CO_2, where species mole fractions at the fuel channel are $H_2 = 0.1$, $H_2O = 0.25$, $CH_4 = 0.5$, CO = 0.14, $CO_2 = 0.01$. A current density of $i = 2$ A cm^{-2}, porosity $\varepsilon = 45\%$, and active catalyst area of 7.5×10^5 m^{-1}, which is used to scale a homogeneous distribution of reformation boundary conditions throughout the structure, are considered. Minima (dark blue) and maxima (dark red) correspond to the minimum and maximum for each species in (f).

Among the more interesting results, the inlet CH_4 and H_2 mole fractions have been systematically varied demonstrating a strong coupling between the structure, transport and reaction processes. This coupling is typical of the processes occurring at similar rates, rather than a rate limited by an individual process. This study suggests the importance of moving to actual SOFC structures which are significantly more complex. It is speculated that the actual anode structure, which contain more complex features, constricted and blind pores, localised catalyst particles and so forth will demonstrate a significant coupling between the structure and the reactive transport. These effects are likely to be exacerbated when transport and reaction are occurring on similar time scales. Additionally, these localised effects and coupling suggest that the extension of the methods to include details related to coking, poisoning and Ni oxidation, are merited. While this will create a numerically stiff problem requiring long, slowly converging solution times, the non-dimensional nature of LBM is amenable and provides a convenient closed framework. These details may be explored in future efforts.

Acknowledgments

Nomenclature

a, b, c, d	stoichiometric coefficients
A, B, C, D	species
A_{Coef}	non-dimensional catalytically active area scalar
$A_{Ni-Pore}$	catalytically active area (lu^{-1} or m^{-1})
A^*	non-dimensional catalytically active area
C	concentration (mol lu^{-3} or mol m^{-3})
D	domain depth (lu or m)
$D_{i,j}$	molecular diffusion coefficient (lu^2 lt^{-1} or m^2 sec^{-1})
e_i^a	lattice velocity for species i, direction a
f_i^a	particle distribution function (PDF) for species i, direction a
F	Farday's constant, 96 485 C mol^{-1}
H	domain height (lu or m)
i	current density (A m^{-2})
J_i	molar flux (mol lu^{-2} lt^1 or mol m^{-2} sec^{-1})

J^*	non-dimensional flux
L	length (lu or m)
MW	molecular mass (kg $kmol^{-1}$)
n	number density (lu^{-3} or m^{-3})
N	count
P	pressure (N m^{-2})
R	universal gas constant, 8.3144 J mol^{-1} K^{-1}
t	time (lt or sec)
T	temperature (K)
u	velocity (lu^2 lt^{-1} or m^2 sec^{-1})
x	mole fraction of species i
X, Y, Z	Cartesian directions

Greek Symbols:

a	LBM unit direction vector
Γ	catalytic site density (mol m^{-2})
ε	porosity (%)
θ_i	surface intermediate surface coverage
v	kinematic viscosity (lu^2 lt^{-1} or m^2 sec^{-1})
ρ	density (kg m^{-3})
τ	tortuosity
τ_i^v	viscous relaxation time for species i
$\tau_{i,j}^D$	diffusive relaxation time for species i,j
Ψ	porosity–tortuosity factor structural constant
Ω_i^a	collision integral for species i, direction a

Subscripts:

Act	active
Coef	coefficient
i, j	species indicators
Ni	catalyst surface
Phys	physical units
LBM	Lattice Boltzmann method units
T	total

Superscripts:

*	non-dimensional
0, eq	equilibrium
a	LBM unit direction vector
D	diffusion
Far	faradaic process
g	gas phase
Ref	reformation process
v	viscous

References

[1] E. Fontell, T. Phan, T. Kivisaari, K. Keranen, *ASME J. Fuel Cell Sci. Technol.* **2006**, *3*, 242.

[2] S. C. Singhal, K. Kendall, Eds. in *High-Temperature Solid Oxide Fuel Cells: Fundamentals, Design and Applications*,

Elsevier Advanced Technology, Oxford, **2003**.■Please provide the page number for all book references.■

[3] F. N. Cayan, M. Zhi, S. R. Pakalapati, I. Celik, N. Wu, R. Gemmen, *J. Power Sources* **2008,** *185*, 595.

[4] A. O. Omosun, A. Bauen, N. P. Brandon, C. S. Ajiman, D. Hart, *J. Power Sources* **2004**, *131*, 96.

[5] J. Mermelstein, M. Millan, N. P. Brandon, *Chem. Eng. Sci.* **2009**, *64*, 492.

[6] R. J. Kee, H. Zhu, A. M. Sukeshini, G. S. Jackson, *Combust. Sci. Technol.* **2008**, *180*, 1207.

[7] G. K. Gupta, J. R. Marda, A. M. Dean, A. M. Colclasure, H. Zhu, R. J. Kee, *J. Power Sources* **2006**, *162*, 553.

[8] R. J. Kee, H. Zhu, D. G. Goodwin, *30th International Symposium on Combustion,* **2005**, 2379.

[9] S. McIntosh, R. J. Gorte, *Chem. Rev.* **2004**, *104*, 4845.

[10] O. Costa-Nunes, R. J. Gorte, J. M. Vohs, *J. Power Sources* **2005**, *141*, 241.

[11] M. Pillai, Y. Lin, H. Zhu, R. J. Kee, S. A. Barnett, *J. Power Sources* **2001**, *195*, 271.

[12] S. McIntosh, H. He, S.-I. Lee, O. Costa-Nunues, V. V. Krishnan, J. M. Vohs, R. J. Gorte, *J. Electrochem. Soc.* **2004**, *151*, A604.

[13] S. McIntosh, J. M. Vohs, R. J. Gorte, *J. Electrochem. Soc.* **2003**, *150*, A470.

[14] M. Zhi, X. Chen, H. Finklea, I. Celik, N. Q. Wu, *J. Power Sources* **2008**, *18*, 485.

[15] A. S. Joshi, K. N. Grew, A. A. Peracchio, W. K. S. Chiu, *J. Power Sources* **2007**, *164*, 631.

[16] W. K. S. Chiu, A. S. Joshi, K. N. Grew, *Euro. Phys. J.: Spec. Top.* **2009**, *171* 159.

[17] K. N. Grew, A. S. Joshi, A. A. Peracchio, W. K. S. Chiu, *J. Power Sources* **2010**, *195*, 2331.

[18] A. S. Joshi, K. N. Grew, J.R. Jr. Izzo, A. A. Peracchio, W. K. S. Chiu, *ASME J. Fuel Cell Sci. Technol.* **2010**, *7*, 011006.

[19] K. N. Grew, Y. S. Chu, Y. Jaemock, A. A. Peracchio, J. R. Jr. Izzo, Y. Hwu, F. DeCarlo, W. K. S. Chiu, *J. Electrochem. Soc.* **2010**, *157*, B783.

[20] J. R. Jr. Izzo, A. S. Joshi, K. N. Grew, W. K. S. Chiu, A. Tkachuk, S. H. Wang, W. Yun, *J. Electrochem. Soc.* **2008**, *155*, B504.

[21] K. N. Grew, A. A. Peracchio, A. S. Joshi, J. R. Jr. Izzo, W. K. S. Chiu, *J. Power Sources* **2010**, doi:10.1016/j.jpowsour.2010.07.005. ■Please provide the Volume and Page number. ■

[22] J. R. Wilson, W. Kobsiriphat, R. Mendoza, H.-Y. Chen, J. M. Hiller, D. J. Miller, K. Thornton, P. W. Voorhees, S. B. Adler, S. A. Barnett, *Nat. Mater.* **2006**, *5*, 541.

[23] Movies available for viewing at: http://www.engr.uconn.edu/me/fuelcellphaseimaging.php.

[24] J. R. Wilson, S. A. Barnett, *Electrochem. Solid State Lett.* **2008**, *11*, B181.

[25] P. R. Shearing, J. Golbert, R. J. Chater, N. P. Brandon, *Chem. Eng. Sci.* **2009**, *64*, 3928.

[26] D. Gostovic, J. R. Smith, D. P. Kundinger, K. S. Jones, E. D. Wachsman, *Electrochem. Solid State Lett.* **2007**, *10*, B214.

[27] H. Iwai, N. Shikazono, T. Matsui, H. Teshima, M. Kishimoto, R. Kishida, D. Hayashi, K. Matsuzaki, D. Kanno, M. Saito, H. Muroyama, K. Eguchi, N. Kasagi, H. Yoshida, *J. Power Sources* **2010**, *195*, 955.

[28] J. R. Wilson, M. Gameiro, K. Mischaikow, W. Kalies, P. W. Voorhees, S. A. Barnett, *Microsc. Microanal.* **2009**, *15*, 71.

[29] R. B. Bird, W. E. Stewart, E. N. Lightfoot, *Transport Phenomena*, John Wiley & Sons, New York, **2002**.

[30] E. L. Cussler, *Diffusion: Mass Transfer in Fluid Systems,* Cambridge University Press, New York, **1997**.

[31] R. J. Kee, M. E. Coltrin, P. Glarborg, *Chemically Reacting Flow: Theory and Practice*, Wiley-Interscience, Hoboken, NJ, **2003**.

[32] J. O. Hirschfelder, C. F. Curtiss, R. B. Bird, *Molecular Theory of Gases and Liquids*, Wiley, New York, **1954**.

[33] E. A. Mason, A. P. Malinauskas in *Gas Transport in Porous Media: The Dusty-Gas Model*, Chemical engineering monographs, Vol. 17, Elsevier Scientific Pub. Co., New York, **1983**.

[34] A. S. Joshi, A. A. Peracchio, K. N. Grew, W. K. S. Chiu, *J. Phys. D* **2007**, *40*, 2961.

[35] D. A. Bader, *Petascale Computing: Algorithms and Applications*, Chapman & Hall, Boca Raton, **2008**.

[36] P. Asinari, M. C. Quaglia, M. R. Von Spakovsky, B. V. Kasula, *J. Power Sources* **2007**, *170*, 359.

[37] P. Asinari, *Phys. Rev. E* **2008**, *77*, 056706.

[38] B. E. Poling, J. M. Prausnitz, J. P. O'Connell, *The Properties of Gases and Liquids,* McGraw-Hill, New York, **2001**.

[39] X. Shan, G. Doolen, *Phys. Rev. E* **1996**, *54*, 3614.

[40] E. S. Hecht, G. K. Gupta, H. Zhu, R. J. Kee, L. Maier, O. Deutschmann, *Appl. Catal. A* **2005**, *295*, 40.

[41] G. M. Goldin, H. Zhu, R. J. Kee, D. Bierschenk, S. A. Barnett, *J. Power Sources* **2009**, *187*, 123.

[42] S. C. DeCaluwe, H. Zhu, R. J. Kee, G. S. Jackson, *J. Electrochem. Soc.* **2008**, *155*, B538.

[43] J. Golbert, C. S. Adjiman, N. P. Brandon, *Ind. Eng. Chem. Res.* **2008**, *47*, 7693.

[44] H. Zhu, R. J. Kee, M. R. Pillai, S. A. Barnett, *J. Power Sources* **2008**, *183*, 143.

[45] W. G. Bessler, S. Gewies, M. Vogler, *Electrochim. Acta* **2007**, *53*, 1782.

[46] H. Zhu, R. J. Kee, V. M. Janardhanan, O. Deutschmann, D. G. Goodwin, *J. Electrochem. Soc.* **2005**, *152*, A2427.

[47] D. G. Goodwin, H. Zhu, R. J. Kee, V. M. Janardhanan, O. Deutschmann, *Meeting Abstracts – 205th Meeting of The Electrochemical Society,* **2004**.

[48] W. H. Press, *Numerical Recipes in Fortran 77: The Art of Scientific Computing*, Cambridge University Press, Cambridge, England, **1996**.

[49] S. Sunde, *J. Electrochem. Soc.* **1996**, *143*, 1930.

[50] S. Sunde, *J. Electrochem. Soc.* **1996**, *143*, 1123.

[51] D. Chen, Z. Lin, H. Zhu, R. J. Kee, *J. Power Sources* **2009**, *191*, 240.

[52] P. Costamagna, P. Costa, V. Antonucci, *Electrochim. Acta* **1998**, *43*, 375.

[53] V. M. Janardhanan, O. Deutschmann, *Chem. Eng. Sci.* **2007**, *62*, 5473.

[54] A. S. Joshi, A. A. Peracchio, K. N. Grew, W. K. S. Chiu, *J. Phys. D* **2007**, *40*, 7593.

[55] N. Epstein, *Chem. Eng. Sci.* **1989**, *44*, 777.

[56] V. H. Schmidt, C.-L. Tsai, *J. Power Sources* **2008**, *180*, 253.

[57] F. Zhao, A. V. Virkar, *J. Power Sources* **2005**, *141*, 79.

[58] Y. Jiang, A. V. Virkar, *J. Electrochem. Soc.* **2003**, *150*, A942.